



PCCP

Hydration structure and water exchange kinetics at xenotime-water interfaces: Implications for rare earth minerals separation

Journal:	<i>Physical Chemistry Chemical Physics</i>
Manuscript ID	CP-ART-01-2020-000087.R1
Article Type:	Paper
Date Submitted by the Author:	20-Feb-2020
Complete List of Authors:	Roy, Santanu; Oak Ridge National Laboratory, Chemical Sciences Division Wu, Lili; University of California at Davis, NEAT ORU and Thermochemistry Facility Goverapet Srinivasan, Sriram; Tata Research Development and Design Center, Physical Sciences Research Area Stack, Andrew; Oak Ridge National Laboratory, Chemical Sciences Division Navrotsky, Alexandra; University of California at Davis, NEAT ORU and Thermochemistry Facility Bryantsev, Vyacheslav; Oak Ridge National Laboratory, Chemical Sciences Division

SCHOLARONE™
Manuscripts

Cite this: DOI: 00.0000/xxxxxxxxxx

Hydration structure and water exchange kinetics at xenotime-water interfaces: Implications for rare earth minerals separation^{†*}Santanu Roy,^{*a} Lili Wu,^b Sriram G. Srinivasan,^{a¶} Andrew G. Stack,^a Alexandra Navrotsky,^{*b‡} and Vyacheslav S. Bryantsev^{*a}

Received Date

Accepted Date

DOI: 00.0000/xxxxxxxxxx

Hydration of surface ions gives rise to structural heterogeneity and variable exchange kinetics of water at complex mineral-water interfaces. Here, we employ *ab initio* molecular dynamics (AIMD) simulations and water adsorption calorimetry to examine the aqueous interfaces of xenotime, a phosphate mineral that contains predominantly Y^{3+} and heavy rare earth elements. Consistent with natural crystal morphology, xenotime is predicted to have a tetragonal prismatic shape, dominated by the {100} surface. Hydration of this surface induces multilayer interfacial water structures with distinct OH orientations, which agrees with recent crystal truncation rod measurements. The exchange kinetics between two adjacent water layers exhibits a wide range of underlying timescales (5-180 picoseconds), dictated by ion-water electrostatics. Adsorption of a bidentate hydroxamate ligand reveals that {100} xenotime surface can only accommodate monodentate coordination with water exchange kinetics strongly depending on specific ligand orientation, prompting us to reconsider traditional strategies for selective separation of rare-earth minerals.

1 Introduction

Water governs a wide range of chemical and biological processes at complex interfaces. Whether in forming crystals (solid or liquid) from ions (inorganic or organic) driven by nucleation¹⁻³ or in guiding molecular reaction dynamics at their interfaces,⁴⁻⁶ water predominantly mediates the underlying mechanisms. Tuning hydrogen-bonding structures and orientational ordering gives control over dynamics of interfacial water and water-mediated ion transport, which is critical for the development of energy technologies that utilize electrolytes. Furthermore, among varieties of

different energy sources, the demand of sustainable, clean, and renewable sources is rising for the prevention of climate change, where water and minerals containing rare earth elements (REE) are playing integral roles.⁷⁻¹¹ Examples where REE are used include wind and hydropower turbines, solar panels, phosphors for lighting, and electric vehicles.¹²

Despite the high demand for REE in energy applications, their beneficiation (recovery) from ores remains inefficient due to critical challenges for separating REE from the surrounding gangue (waste) materials.¹³⁻¹⁵ For example, Y^{3+} and Ce^{3+} are the major REE that can be respectively found in the xenotime and bastnäsite minerals and associated gangue minerals. Utilizing the fact that these minerals have structurally, dynamically, and energetically distinct surfaces, one can adopt a combined approach of different surface-sensitive experiments and computer simulations to investigate the adsorption and dynamics of water and ligands under relevant hydration conditions. To provide the initial steps toward developing an understanding for selective flotation of rare-earth minerals, here we have conducted density functional theory (DFT)-based optimization and *ab initio* molecular dynamics simulations (AIMD) of hydrated xenotime surfaces. The results provide critical insights into different activated interfacial processes (*i.e.*, events that require overcoming free energy barriers such as water exchange), which are complemented with surface calorimetry of water adsorption and compared with recently reported¹⁶ crystal truncation rod (CTR) measurements.

Typically, froth flotation^{15,17} is employed for the REE benefici-

^a Chemical Sciences Division, Oak Ridge National Laboratory, 1 Bethel Valley Rd., Oak Ridge, TN 37830, USA; E-mail: roys@ornl.gov, bryantsev@ornl.gov

^b Peter A. Rock Thermochemistry Laboratory and NEAT ORU, University of California Davis, 1 Shields Avenue, Davis, CA 95616, USA.

[†] Electronic Supplementary Information (ESI) available: [The details of the DFT-based electronic structure calculations, AIMD, and surface calorimetry measurements are given here.]. See DOI: 00.0000/00000000.

[¶] Present address: TCS Research, Tata Research Development and Design Centre, 54-B Hadapsar Industrial Estate, Hadapsar, Pune-411013, Maharashtra, India.

[‡] Present address: School of Molecular Sciences, The College of Liberal Arts and Sciences, and the School for Engineering of Matter, Transport and Energy, Arizona State University, Arizona, USA., Email: Alexandra.Navrotsky@asu.edu

* This manuscript has been authored in part by UT-Battelle, LLC, under contract DE-AC05-00OR22725 with the US Department of Energy (DOE). The US government retains and the publisher, by accepting the article for publication, acknowledges that the US government retains a nonexclusive, paid-up, irrevocable, worldwide license to publish or reproduce the published form of this manuscript, or allow others to do so, for US government purposes. DOE will provide public access to these results of federally sponsored research in accordance with the DOE Public Access Plan (<http://energy.gov/downloads/doe-public-access-plan>).

ation process, where air bubbles are passed through a water tank containing a mixture of finely ground ore, hydrophobic collector ligands, and suppressor ligands. The role of the collector ligand is to selectively bind to the REE mineral surfaces and render them hydrophobic, whereas suppressor ligands bind to gangue materials and render them hydrophilic. Thereby, while the gangue minerals remain solvated in water, the REE minerals separate from the gangue minerals, and then the air bubbles drive them to the air-water interface at the top of the tank for recovery. The REE separation in froth flotation can be further enhanced through controlling the pH, *i.e.*, exploring different possible protonation states of the ligands and their water-mediated interactions with the mineral surfaces. Thus, water dictates the flotation process as a medium; yet, despite a few recent efforts of examining the stability and structures of REE surfaces,^{16,18–21} a complete, fundamental picture of the interfacial hydration structures and kinetics that are likely to be highly heterogeneous is yet to be described for establishing the connection with REE mineral flotation.

The hydration structures and dynamics of ions in water are highly sensitive to the ionic size and charge. Recent MD simulations^{22–25} showed that smaller ions (e.g., Li^+ , Mg^{2+} , F^-) strongly interact with water and create multiple, well-defined coordination structures, whereas the larger ions (e.g., Cs^+ , Fr^+ , I^- , BF_4^-) weakly interact with water and the resulting coordination states may be poorly resolved. Several X-ray and neutron scattering^{26–30} and X-ray absorption^{31–37} experiments confirmed such diversity of coordination environments of different ions in aqueous solutions. The nature of the ion-water interactions also dictates the water dynamics as revealed by MD simulations and different time-resolved spectroscopic techniques such as dielectric relaxation,³⁸ anisotropy decay in polarization-resolved infrared,^{39,40} and two-dimensional infrared (2DIR)^{41–45} experiments. The findings of these studies establish that water in the hydration shells of strongly-interacting ions exhibit slower hydrogen-bonding and rotational dynamics than bulk water, covering a wide range (sub-picoseconds to microseconds) of underlying timescales.

Recent 2DIR and its surface-sensitive variant, 2D sum frequency generation (2DSFG) spectroscopic studies^{46–49} showed that the interfacial hydration of complex molecules and materials is rather intricate due to several competing driving forces, including local electrostatics, hydrogen-bonding, hydrophobicity, and interfacial curvature that guide the hydration process. For example, strong electric fields from an interface can orient water OH chromophores either away or towards the interface, which can be further influenced by tuning the chemical structures of the interface that may or may not form hydrogen bonds with water.⁴⁶ Strong hydrogen bonds slow down the interfacial water dynamics, which can be changed to faster dynamics if the curvature of the interface is converted to convex.⁴⁷

At mineral interfaces, where multivalent cations and anions are alternatively arranged, multilayering of interfacial hydration structures with different orientational ordering of water molecules due to competition between the cation-water and anion-water electrostatics is expected, but further details remain largely unexplored. Solvent- and ligand-exchange kinetics of min-

eral surfaces have previously been found to correlate with rates of processes such as dissolution on some minerals⁵⁰. However, except in a limited number of cases,^{51–54} the magnitudes of the solvent exchange rates and mechanisms of individual surface sites are poorly constrained. This is in part due to experimental measurements that typically yield a distribution of solvent-exchange rates over all surface sites, rather than surface site-specific ligand exchange rates required to design new, more efficient ligands for REE extraction.

In this article, we demonstrate the ability of AIMD simulations to unravel the complexities of highly heterogeneous interfacial water structures at xenotime mineral interfaces. We show that DFT calculations can accurately predict the surface energy and stability of xenotime in accordance with the surface calorimetry measurements. Furthermore, our study reveals the existence of multilayer water structure at the mineral interface in the fully hydrated state and shows how ligand adsorption influences the exchange kinetics of water between these layers. We are able to portray these phenomena through utilization of our newly established formalism of Marcus theory of water exchange,^{24,25} which shows that solvent rearrangement that breaks and reforms water hydrogen bonds dictates the mechanisms and rates of exchange events. Adsorption studies establish that {100} xenotime surface can only accommodate a monodentate coordination with a bidentate hydroxamate ligand, wherein water exchange kinetics are strongly influenced by the choice of the binding configuration. This information could be used to develop design strategies to enhance flotation selectivity of REE minerals.

Computational Methods

DFT-based structural optimization

Xenotime is an yttrium-dominated phosphate rare earth mineral (nominally, YPO_4) that crystallizes in the tetragonal geometry with $I4_1/amd$ space group symmetry. The structure and stability of the following low-index surfaces was investigated using DFT: {100}, {110}, {101}, and {001}. These calculations were performed using the VASP software,^{55–58} where the plane wave basis was used to describe electronic states and the core-valence interaction was treated using the projector augmented wave (PAW) method.^{59,60} The semicore 4s and 4p states of Y^{3+} were treated as valence states. We set the plane wave kinetic energy cutoff to 600 eV. The Perdew-Burke-Ernzerhof (PBE) generalized gradient approximation (GGA) functional^{61,62} was used to describe the exchange correlation interactions with dispersion correction by Grimme's DFT-D3⁶³ method. Although it is well known that PBE can lead to overstructuring of liquid water,⁶⁴ our recent study¹⁶ comparing PBE-D3 with different more expensive functionals such as PBE0-D3^{63,65} showed that the PBE-predicted microsolvent water structure at the {100} surface were very similar to those obtained using other functionals. Using better functional may quantitatively improve the results without significantly modifying the conclusions of this work.

For the bulk calculations, the Brillouin zone in the bulk calculations was sampled using a $4 \times 4 \times 4$ Monkhorst-Pack k-point mesh. Geometry optimizations allowing relaxation of all atoms

were considered converged when the forces on all of the atoms between two relaxation steps went below $0.01 \text{ eV } \text{Å}^{-1}$. The self-consistent-field (SCF) convergence threshold during optimization was set to 10^{-5} eV . The Pulay mixing scheme⁶⁶ was employed for charge density mixing in the SCF procedure. As shown in our previous work,¹⁶ the predicted lattice parameters ($a = b = 6.9143 \text{ Å}$ and $c = 6.0429 \text{ Å}$) were in excellent agreement with the experiment. Slab models of various surfaces were constructed using the Build surfaces feature in Medea.⁶⁷ The vacuum gap between two surfaces was at least 18 Å . For the optimization of different surfaces with 100% (one water per Y^{3+}) and 200% (two water per Y^{3+}) water coverage, several initial geometries were generated from chemical intuition of ion-water hydrogen-bonding.

DFT-based AIMD

The AIMD simulations of the xenotime-water interface were performed in the Born-Oppenheimer approximation using the VASP software^{55–58} without (for 75 ps) and in the presence of acetohydroxamate (for 45 ps). First 5–10 ps was treated as the equilibration period and the remainder was used for analysis. The DFT protocol was the same as that for the optimization, except the use of the plane wave kinetic energy cutoff of 400 eV and the Γ -point approximation. Note that, the two $\{100\}$ surfaces were represented by the top and bottom layers of a 3-layer slab (with the lattice vectors: $a = 13.829 \text{ Å}$, $b = 12.086 \text{ Å}$, and $c = 42.000 \text{ Å}$, where c is perpendicular to $\{100\}$) that was solvated by a total of 80 water molecules (40 water molecules for each side). We used a vacuum gap of 18 Å to avoid the interaction between two image interfaces along c .

Results and discussion

To examine the stability of different surfaces, the surface energies, E_{surf} , were computed from the difference of the total energies of the slab (E_{S}) and bulk (E_{B}) with equal number of YPO_4 formula units, normalized per surface area (A):

$$E_{\text{surf}} = [E_{\text{S}} - E_{\text{B}} - n_{\text{H}_2\text{O}}(E_{\text{ads}} + G_{\text{H}_2\text{O}})]/2A, \quad (1)$$

where $n_{\text{H}_2\text{O}}$ is the total number of water molecules symmetrically adsorbed on both sides of the slab ($n_{\text{H}_2\text{O}} = 0$ for gas phase calculations) and E_{ads} is the normalized (per water) adsorption energy of water. Taking liquid water as a reference state, the free-energy correction in Equation 1 takes the form $G_{\text{H}_2\text{O}} = -H_{\text{vap}} - TS_{\text{liq}}^0$, where H_{vap} is the water evaporation enthalpy and S_{liq}^0 is the absolute entropy of liquid water. Here, we assume that the entropy of strongly adsorbed water is small and can be ignored. The computed surface energies are presented in Figure 1. The convergence of these energies in each calculation was confirmed by varying the number of layers (*i.e.*, $\text{Y}^{3+}\text{-PO}_4^{3-}$ units) in the slabs and the bulk geometry (see Figure S1 for different surface configurations and Table S1 and Table S2, respectively for the actual values of E_{surf} and E_{ads} and their convergence tests). For 0% water coverage, E_{surf} is the lowest for the $\{100\}$ surface, followed by $\{110\}$, Y^{3+} -truncated and PO_4^{3-} -truncated $\{101\}$, and $\{001\}$ surfaces in ascending order. While this trend persists for 100% water coverage, the surface energy (despite the expected over-

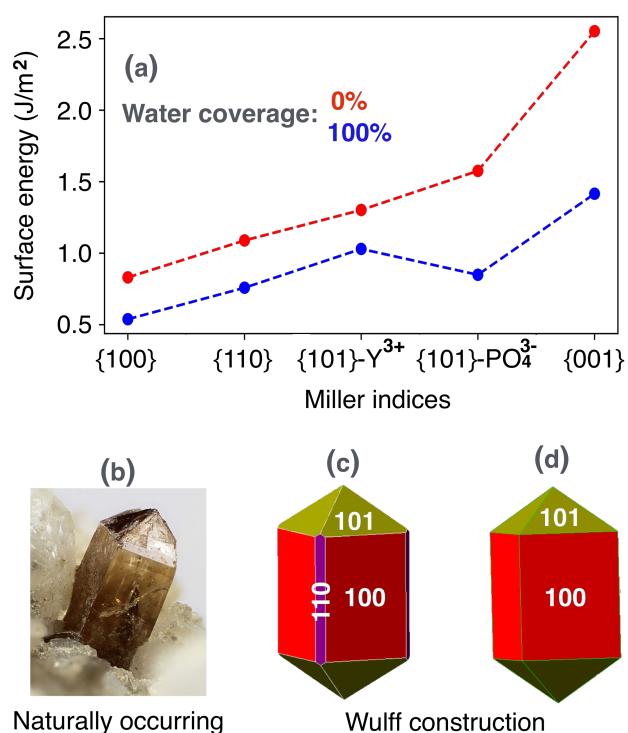


Fig. 1 Xenotime surface energies with varying water coverage (a). The resemblance between the naturally occurring crystal structure (b) and the crystal morphology obtained from the Wulff construction method⁶⁸ at 0% (c) and 100% (d) water coverage is excellent. The image for the naturally occurring crystal structure was taken from mindat.org with the permission from Matteo Chinellato.

estimation due to the neglect of the entropy of adsorbed water molecules) decreases significantly due to stabilization by water adsorption.

As evident from Figure 1b, the morphology of the naturally occurring xenotime crystals is dominated by the most stable $\{100\}$ surface. The Wulff method,⁶⁸ used to construct an equilibrium shape of a crystal by minimizing its surface energy, reproduces the prismatic tetragonal form of xenotime and identifies different crystal facets shown in Figure 1c. To compare surface energies with the experimental values obtained by adsorption calorimetry (see ESI), we calculated surface area-weighted surface energy ($E_{\text{Surf}} = 1.02 \text{ J/m}^2$) for 0% water coverage, which agrees well with the value, $E_{\text{Surf}} = 1.16 \text{ J/m}^2$ measured by us using surface calorimetry. While the $\{100\}$, $\{110\}$, $\{101\}$ surfaces are clearly identified for the 0% water coverage, the 100% water coverage leads to the existence of only the $\{100\}$ and $\{101\}$ surfaces in the crystal morphology. The dominant $\{100\}$ surface therefore entails more in-depth investigation as the most relevant surface to target in the design of flotation agents.

Figures 2a and 2b depict the interfacial hydration structure of the $\{100\}$ surface for the 100% and 200% water coverage optimized via DFT calculations. Water molecules are located on top of the cations and anions, forming hydrogen bonds between themselves and with the surface ions. However, the AIMD simulation shows a drastic change in the hydration structure due to the increased water coverage of 500% and the dynamical effects arising

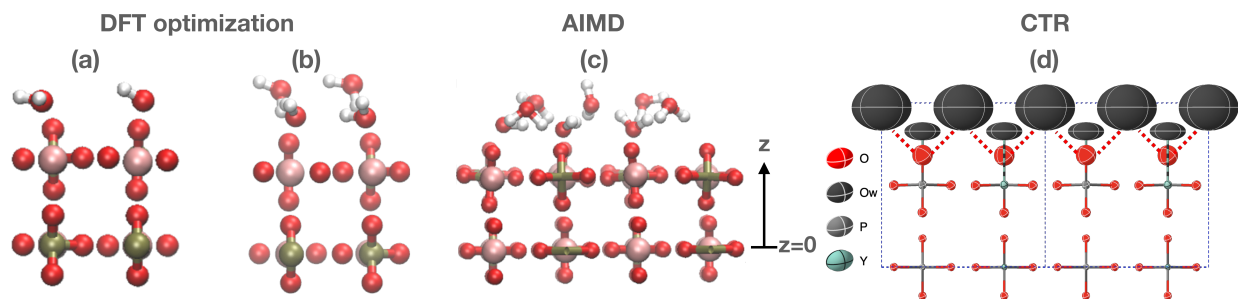


Fig. 2 DFT-optimized atomic structure of {100} xenotime surface (only top two layers are shown) at 100% (a) and 200% (b) water coverage. The equilibrium locations of water molecules in the completely solvated state (500% water coverage) from the AIMD simulations, where only the first two water layers are shown for clarity in the AIMD snapshot (c). Pink, golden green, red, and white indicate respectively Y, P, O, and H in a, b, and c. AIMD simulations give a more correct portrayal of the interface, consistent with the reported CTR measurements¹⁶ (d), where the PO_4^{3-} -bound water molecules are between the PO_4^{3-} groups and the Y^{3+} -bound water molecules are on top of Y^{3+} ions.

from the thermal equilibrium at 300K. These simulations are performed for about 75 ps using a three-layer slab (see ESI for the AIMD simulation protocol) that has two {100}-water interfaces located at the top and bottom of the slab. We find that on average (considering the last 70 ps as the production run) while the Y^{3+} -bound water molecules with OH chromophores pointing away the interface fluctuate at the top of Y^{3+} , the PO_4^{3-} -bound water molecules rearrange to find their equilibrium locations between the PO_4 groups and their OH chromophores point towards the interface (Figure 2c). This is in excellent agreement with the CTR measurements (Figure 2d) reported in our earlier work.¹⁶ Furthermore, according to the AIMD simulations, the equilibrium distance between Y^{3+} and water oxygen is shorter ($2.37 \pm 0.13 \text{ \AA}$) than the equilibrium distance between PO_4^{3-} and water oxygens ($2.72 \pm 0.18 \text{ \AA}$), confirming the existence of two distinct adjacent layers of interfacial water. The CTR measurements validate such findings by reproducing these equilibrium distances in a reasonably good agreement (within the errors of simulated results): 2.28 \AA and 2.65 \AA , respectively for the Y^{3+} -water oxygen and PO_4^{3-} oxygen-water oxygen distances. By comparing Figures 2b and 2d, we notice that static DFT calculations fail to correctly predict the positions of the second layer water molecules that are shifted by about half a unit cell (when viewed along the {001} direction) with respect to the CTR structure. Thus, it is evident that the AIMD simulation with abundant water coverage of the interface is necessary to correctly portray xenotime-water interface, explaining the previous discrepancy¹⁶ between the DFT and CTR structures.

The multilayers of hydration structure can be resolved as the thermodynamically stable states on a free energy surface. From the AIMD simulations we compute the two-dimensional free energy surface, $W(z, n)$, as a function of the distance (z) from the central layer and the number of water-water hydrogen bonds, *i.e.*, coordination number (n) of a water molecule with other water molecules. n is defined as:²⁴

$$n = \sum_{i=1}^{N_W-1} \frac{1 - (r_i/r^\ddagger)^{12}}{1 - (r_i/r^\ddagger)^{24}}, \quad (2)$$

where r_i is the distance between the i^{th} water molecule and a select water molecule for which n is obtained. N_W is the total

number of water molecules and r^\ddagger is the location of the first minimum of the radial distribution function (RDF) for the distances between water oxygens, representing the boundary between the first and second solvation shells. The water-water hydrogen-bonding network present in the bulk environment is likely to break down at the interfacial environment due to interaction with the surface ions, leading to a reduced water-water coordination number that allows us to distinguish the interfacial water from the bulk water in the coordination number space. As shown in Figure 3, the 2D-free energy surface clearly distinguishes three distinct layers of water in terms of three minima as moving away from the interface (*i.e.*, as z increases): The interfacial water in the Y^{3+} -bound (Layer 1) and PO_4^{3-} -bound (Layer 2) states with $n \sim 3 - 4$ and the bulk-like water (Layer 3) with $n \sim 4 - 5$. Such partitioning of water is consistent with water adsorption calorimetry, indicating that at about $9.0 \text{ H}_2\text{O}/\text{nm}$ coverage (corresponding to Layer 1 and Layer 2), water is strongly bound and can be considered chemisorbed, while the remaining water can be treated as physisorbed water (Section 2 in the ESI). Furthermore, our finding about the fluctuating water-water coordination number in this physisorbed bulk-like water ($n \sim 4 - 5$) is in good agreement with the different neutron diffraction measurements on liquid water⁶⁹ that determined the average water-water coordination number of 4.3-4.4 by integrating the oxygen-oxygen RDF up to the first minimum.

The 1D free energy, $W(z)$, obtained by integrating $W(z, n)$ over n , $\exp[-W(z)/k_B T] = \int \exp[-W(z, n)/k_B T] dn$, shows the presence of much larger free energy barriers than thermal energy (0.6 cal/mol) along the z direction (Figure 3a). Thus, the transitions between different interfacial hydration layers are rare events. To examine these rare events, we adopt Marcus theory of solvent exchange^{24,25} that describes a 2D-pathway for water molecules to transit from Layer 1 to Layer 2, and then to Layer 3 through a series of water exchange processes (the white and red arrows on the 2D-free energy surface). Marcus theory reveals that solvent rearrangement activates and drives the reactant coordination state of a water molecule in Layer 1 to the state of higher coordination number that enables its spontaneous (barrier-less) departure along z towards the product state in Layer 2. Also, the transition from Layer 2 to Layer 3 is driven by the same mechanism.

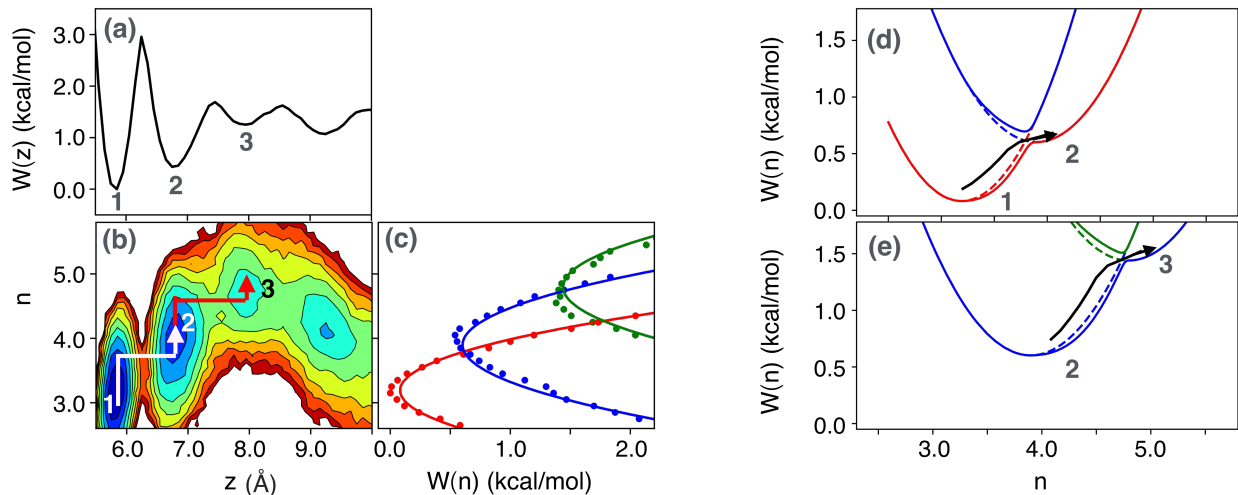


Fig. 3 The free energies, $W(z)$ (a), $W(z,n)$ (b), and $W(n)$ (c) indicating different hydration layers (Layer 1, Layer 2, and Layer 3) in terms of the free energy minima. The arrows on the 2D-surface represent the Marcus pathways for the transitions between these layers. 10 contours on $W(z,n)$ are placed between 0 and 3.5 kcal/mol. For $W(n)$, the dotted lines are extracted values, whereas the solid lines are parabolic fits. Generation of lower and higher eigen free energy surfaces caused by the coupling between the reactant and product Marcus parabolas, showing the adiabatic traversal of the crossing point (d and e).

To determine the rates of transitions between the hydration layers using Marcus theory, we extract the slices from $W(z,n)$ along the equilibrium locations ($z = z_R$ and $z = z_P$) of the reactant (R) and product (P) states and model them as the parabolic functions of n :

$$\begin{aligned} W(z_R, n) &= W_R(n) = \frac{1}{2} K_R n^2 \\ W(z_P, n) &= W_P(n) = \frac{1}{2} K_P (n - n_P)^2 + \Delta W, \end{aligned} \quad (3)$$

where K_R and K_P are the curvatures of the reactant and product parabolas with the minima, $n = 0$ and $n = n_P$, respectively. ΔW is the free energy difference between the product and reactant equilibria ($W_P(n_P) - W_R(0)$). We separately examine the Layer 1 to Layer 2 and Layer 2 to Layer 3 transitions; therefore, Layer 2 is a product in the former while it is a reactant in the latter. As Figure 3c displays, the reactant and product parabolas are the diabatic states that cross at a point treated as the transition state – which is essentially the aforementioned overcoordinated state on the Marcus pathways on the 2D-free energy surface (Figure 3b). Since these parabolas cross at the “normal region” (opposite side), the reactant-to-product transition can be treated as the adiabatic traversal of the crossing point. That is, since the coupling between the Marcus parabolas generate a lower and a higher eigen free energy surface, the adiabatic dynamics on the lower free energy surface (Figure 3d) can describe this transition.^{24,25,70} The associated free energy barrier depends on the free energy difference, ΔW , solvent reorganization energy, λ (energy cost for changing the equilibrium reactant to the equilibrium product states, $\lambda = W_R(n_P) - W_R(0)$), and the curvature difference

($\Delta K = K_R - K_P$) between the parabolas:²⁴

$$\begin{aligned} \Delta W^\ddagger &= \frac{K_P(K_R + K_P)}{\Delta K^2} \lambda + \frac{K_R}{\Delta K} \Delta W \\ &\quad - \frac{\sqrt{2n_P K_R K_P}}{\Delta K^2} \sqrt{[K_P \lambda + \Delta K \Delta W]} \end{aligned} \quad (4)$$

The assumption that as soon as the system arrives at the crossing point from the reactant state it spontaneously goes to the product state may not be always true. For example, the barrier along z at the crossing point, which is presumably set to zero, might have a small but unignorable value ($\Delta W_z^{n^\ddagger}$). Furthermore, trajectories might recross the transition state due to the dynamical non-equilibrium solvent effects^{71–76} on n . Therefore, only a fraction of the trajectories actually crosses the transition state and arrives at the product, which is obtained through computing the transmission coefficient. The semiclassical approach by Landau and Zener^{77–80} showed that the transmission coefficient, κ_{LZ} , depends on the probability (P) of the reactive transition through the crossing point of the Marcus parabolas. When the crossing point is located at the “normal region”, $\kappa_{LZ} = 2P/(P+1)$. P is governed by the coupling (C) between the parabolas and the traversal velocity (v_n) at the crossing point: $P = 1 - \exp\left[-\frac{2\pi C^2}{\hbar v_n |S_2 - S_1|}\right]$, where $S_{1,2} = \frac{dW(n)}{dn}|_{n=n^\ddagger}$ are the slopes of the parabolas at the crossing point and $\hbar = h/2\pi$ (h is the Planck constant). The velocities are exponentially distributed at the crossing point and v_n is obtained from the mean value of the distribution. C is obtained at $n = n^\ddagger$ as, $C(n) = \frac{K_R + K_P}{2\sqrt{K_R K_P}} \sqrt{[W_R(n) - W_R(0)][W_P(n) - W_P(n_P)]}$.^{24,25,70} Now, after incorporating the small barrier along z ($\Delta W_z^{n^\ddagger}$) in addition to ΔW^\ddagger at the transition state and the transmission coefficient (κ_{LZ}), the Marcus rate expression takes the form of:^{24,25,70}

$$k_{\text{Marcus}} = \kappa_{LZ} \frac{k_B T}{h} \exp[-(\Delta W^\ddagger + \Delta W_z^{n^\ddagger})/k_B T]. \quad (5)$$

While all the parameters used in the Marcus model are listed in the ESI (Table S4), the essential ones such as the barriers, transmission coefficients, and transition timescales ($\tau = 1/k_{\text{Marcus}}$) are given in Table 1. The timescale for the transition from Layer 1 to Layer 2 is one order magnitude (~ 145 picoseconds (ps)) slower than that for the Layer 2-to-Layer 3 transition (~ 19 ps). This is because the former is associated with a larger barrier, a total of ~ 3 cal/mol due to stronger Y^{3+} -water interactions, whereas the latter experiences a twice smaller total barrier due to weaker PO_4^{3-} -water interactions. More recrossing events (smaller κ_{LZ}) may cause a little slowing down of the Layer 2-to-Layer 3 transition as compared to the Layer 1-to-Layer 2 transition, but here such effects are much less significant than the barrier effects. It should be noted that water exchange around a surface Y^{3+} ions (*i.e.*, the Layer 1-to-Layer 2 transition) is much faster than water exchange around a multivalent rare earth cation in the bulk water that occurs typically on the nanosecond or slower timescales.⁸¹ This is due to weakening of the cation-water electrostatics at the interface by the neighboring phosphate anions.

Table 1 Barrier, transmission coefficient, and timescale for the transition from Layer 1 to Layer 2 and from Layer 2 to Layer 3 obtained using Marcus theory of solvent exchange.

	Xenotime-water	Config A	Config B
1→2 transition			
$\Delta W^\ddagger + \Delta W_z^{n\ddagger}$ (kcal/mol)	2.97	3.31	2.66
κ_{LZ}	0.17	0.50	0.08
τ (ps)	144.63	86.17	175.76
2→3 transition			
$\Delta W^\ddagger + \Delta W_z^{n\ddagger}$ (kcal/mol)	1.40	1.91	1.31
κ_{LZ}	0.09	0.46	0.45
τ (ps)	19.19	8.65	3.29

Selective adsorption of surfactants at the mineral-water interface imparts surface hydrophobicity, which is directly related to mineral flotation efficiency. We note that building realistic models of anionic ligands adsorption at mineral-water interfaces presents a significant challenge, because one must rigorously avoid spurious charge-charge interactions across supercell boundaries. The most physically justifiable, but computationally expensive approach is to include explicit counterions in a solvent medium, where both anionic ligand and counterions are fully hydrated. Hydroxamic acid in the deprotonated form was chosen as a prototypical ligand, because as a primary functional group, it is employed for the selective flotation of rare earths ore in large scale industrial plants.¹⁵ Hydroxamate has two binding groups, namely, the C=O and N-O⁻ sites (Figure 4a and 4b). AIMD simulations were initiated from two starting configurations (Config A and Config B) together with the counterion Na⁺, where in Config A the ligand interacts with Y³⁺ through the N-O⁻ binding site in a monodentate configuration, while in Config B both C=O and N-O⁻ interact with Y³⁺ in a bidentate chelate configuration. However, the chelate mode was unstable and converted

into a monodentate mode during the first 5 ps of AIMD simulation, wherein the C=O site remained bound to Y³⁺, but the N-O⁻ site lost attachment to the surface and got fully exposed to water (Figure S2). The counter ion, Na⁺, was initially located away from both the ligand and the interface. It remained there for Config A, while it moved to stay in close proximity to N-O⁻ in Config B. After the production stage of 40 ps, the RDF ($g(r)$) and the integrated $g(r)$, *i.e.*, the number of water molecules around the binding sites ($n(r)$), depicted in Figure 4c confirm that, when a binding site (C=O or N-O⁻) is away from the surface, it forms a well-defined hydration shell around it by forming 2-3 hydrogen bonds with water. However, there is a drastic difference between the hydration structure of N-O⁻ and C=O when they bind to the surface. The N-O⁻ group in Config A attracts water molecules towards the ligand-surface contact point and in this hydrophilic environment it clearly forms a hydrogen bond with water. The C=O group hardly interacts with water at the contact point (ignorable peak height of $g(r)$ and vanishingly small value of $n(r)$), and thus creates mild hydrophobicity around it. Additional interaction with water molecules is the likely reason why the ligand O-Y³⁺ distance in Config A is slightly longer ($2.32 \pm 0.09 \text{ \AA}$) than in Config B ($2.28 \pm 0.12 \text{ \AA}$).

The ligand-induced perturbation of the hydration structure at the interface has a significant impact on the interfacial water exchange kinetics. Figure S3 and S4 display how the Marcus pathways of the transitions between different hydration layers get affected by the ligand in different binding configurations. The Layer 1-to-Layer 2 transition is now a nonadiabatic process since the Marcus parabolas cross at the "abnormal region", *i.e.*, the transition is guided by the nonadiabatic jump from the lower to higher eigen free energy surface through this crossing point (Figure S4e and S4f). The transmission coefficient is determined in this case as $\kappa_{LZ} = 2P(P-1)$. As listed in Table 1, the timescale for the transition from Layer 1 to Layer 2 gets faster (86 ps) in Config A and slower (176 ps) in Config B. Here the effect from the total barrier is less significant than the transmission coefficient, since the latter changes much more drastically as going from Config A to Config B. The abundance of water near the contact point in Config A favors the water exchange and prevents barrier-recrossing as indicated by the larger transmission coefficient. On the contrary, the lack of enough water near the contact point in Config B imposes resistance against the exchange, causing significant barrier-recrossing as gleaned from the very small transmission coefficient. Thus, effectively, Config B causes slower exchange dynamics of water between Layer 1 and Layer 2. The Layer 2-to-Layer 3 transition gets 2-5 times faster when the ligand interacts with the surface regardless of their binding configurations (Table 1) because the ligand replaces the water molecules at the contact point in Layer 1, which move to the 2nd or 3rd layer increasing the availability of water needed for the exchange. This causes significant increase in the transmission coefficient that results in faster exchange. Config B draws most of the interfacial water towards Layer 2 or Layer 3, thus inducing the fastest Layer 2-to-Layer 3 transition.

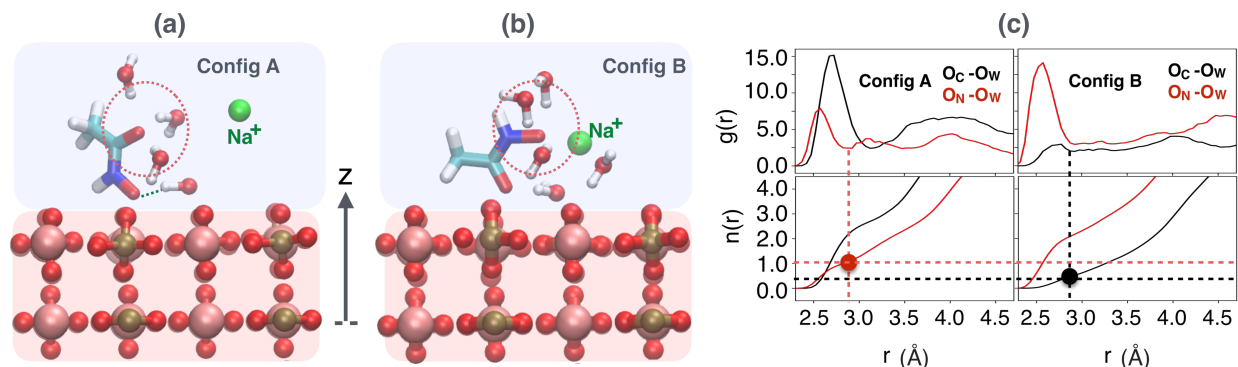


Fig. 4 AIMD snapshots of two binding configurations of acetohydroxamate at the water-xenotime interface (a and b), showing that the N-O^- group binds to the surface as well as forms a hydrogen bond (green dashed line) with a water molecule (Config A), whereas the C=O group binds to the $\{100\}$ surface without forming a hydrogen bond with water (Config B). The unbound C=O/N-O^- group forms hydrogen bonds with 2-3 water molecules (indicated by red circles). The radial distribution function for the binding site-water oxygen (O_w) distance together with the number of water molecules, $n(r)$, around the binding sites for Config A and Config B (c).

2 Conclusion

In summary, we have presented an in-depth picture of interfacial hydration structure and water exchange kinetics at xenotime mineral interfaces by employing a combined approach of DFT calculations, AIMD, and surface calorimetry. Through DFT calculations we have accurately predicted the naturally occurring crystal morphology of xenotime in the gas and microsolvated phases that comprise mostly the $\{100\}$ and $\{101\}$ surfaces. Ensemble average of high coverage of water using AIMD simulations allowed us to acquire a more accurate portrayal of the atomic ordering at the interface and obtain a precise agreement with the CTR best-fit model. The most dominating surface, $\{100\}$, displays a thermodynamically stable multilayer interfacial hydration structure. It is divided into three layers on the 2D-free energy surface when projected along the distance from the interface and the water-water coordination number. By employing Marcus theory that utilizes this 2D-free energy surface, we find that the water exchange kinetics are also heterogeneous - the Layer 1-to-Layer 2 transition is ~ 8 time slower than the Layer 2-to-Layer 3 transition, as the former faces much larger barrier due to the Y^{3+} -water interaction that is stronger than the PO_4^{3-} -water interaction. The largest reported timescale (~ 176 ps) is greater than the actual simulation time. It is an asymptotic estimation by Marcus theory, which can be evaluated if one is able to construct the diabatic reactant and product Marcus parabolas with a well-defined crossing point. Obtaining these timescales by using other methods, such as calculating the time-correlation functions of the probability of finding a water molecules in a hydration shell,⁸² will require infeasible AIMD trajectories of nanoseconds length. For the experimental validation of our finding about the interfacial water dynamics, the surface-sensitive 2DSFG spectroscopy can be employed as elucidated by several recent studies on air-water⁸³ and lipid-water interfaces.^{46,48}

Knowledge of the precise positions of water on xenotime can facilitate informed ligand design for improved flotation of REE-bearing ores. In this work, we have employed AIMD simulations to model adsorption of a hydroxamate ligand on the $\{100\}$ surface. We find that hydroxamate, which normally forms chelate

complexes with trivalent lanthanide ions in solution, prefers to adsorb on the $\{100\}$ xenotime surface in the monodentate configuration, either through the C=O or N-O^- site. Since only one Y-O-PO_3 bond is broken upon forming the $\{100\}$ xenotime surface, forcing a higher coordination number in a chelate complex of surface Y^{3+} compare to bulk Y^{3+} is apparently energetically unfavorable. This is quite different from adsorption on the $\{100\}$ bastnäs site surface, where surface lanthanide ions have three broken bonds and can easily accommodate bidentate chelation.¹⁴ Thus, the emerging strategy for improving selectivity for xenotime over gangue minerals is to replace a single chelating group with multiple monodentate groups that are positioned to complement and simultaneously interact with several adjacent surface sites. An improved understanding of these ligand-mineral surface interactions can be achieved through exploration of adsorption free energy landscapes for different binding configurations of ligands at different orientations. As both the structure and exchange kinetics of water at mineral surfaces are highly sensitive to the very nature of ligand-mineral surface interactions, there is additional possibility to fine-tune surface hydrophobicity by exploiting differences in the interfacial hydration structure and water exchange kinetics imposed by different binding sites.

Conflicts of interest

There are no conflicts to declare.

Acknowledgements

This work was supported by the Critical Materials Institute, an Energy Innovation Hub funded by the U.S. Department of Energy, Office of Energy Efficiency and Renewable Energy, Advanced Manufacturing Office and used resources of the Oak Ridge Leadership Computing Facility and National Energy Research Scientific Computing Center (NERSC, U.S. Department of Energy Office of Science User Facility), which are respectively operated under Contract No. DE-AC05-00OR22725 and DE-AC02-05CH11231.

Notes and references

- 1 S. Price, S. Veessler, H. Pan, K. Lewtas, M. Smets, B. Rimez, A. Myerson, C. Hughes, A. Hare, F. Zhang and et al., *Faraday*

- Discuss.*, 2015, **179**, 155–197.
- 2 S. A. Deshmukh, L. A. Solomon, G. Kamath, H. C. Fry and S. K. R. S. Sankaranarayanan, *Nature Communications*, 2016, **7**, 12367.
 - 3 G. C. Sosso, J. Chen, S. J. Cox, M. Fitzner, P. Pedevilla, A. Zen and A. Michaelides, *Chem. Rev.*, 2016, **116**, 7078–7116.
 - 4 O. Björneholm, M. H. Hansen, A. Hodgson, L.-M. Liu, D. T. Limmer, A. Michaelides, P. Pedevilla, J. Rossmeisl, H. Shen, G. Tocci and et al., *Chem. Rev.*, 2016, **116**, 7698–7726.
 - 5 N. Laanait, E. B. R. Callagon, Z. Zhang, N. C. Sturchio, S. S. Lee and P. Fenter, *Science*, 2015, **349**, 1330–1334.
 - 6 C. V. Putnis and E. Ruiz-Agudo, *Elements*, 2013, **9**, 177–182.
 - 7 P. S. Arshi, E. Vahidi and F. Zhao, *ACS Sustainable Chemistry & Engineering*, 2018, **6**, 3311–3320.
 - 8 T. Dutta, K.-H. Kim, M. Uchimiya, E. E. Kwon, B.-H. Jeon, A. Deep and S.-T. Yun, *Environmental Research*, 2016, **150**, 182 – 190.
 - 9 S. M. M. Ehteshami and S. Chan, *Energy Policy*, 2014, **73**, 103 – 109.
 - 10 S. Chu, Y. Cui and N. Liu, *Nature Materials*, 2016, **16**, 16–22.
 - 11 N. Panwar, S. Kaushik and S. Kothari, *Renewable and Sustainable Energy Reviews*, 2011, **15**, 1513 – 1524.
 - 12 2011 U.S. Department of Energy Strategic Plan., U.S. Department of Energy: Washington D.C., Web. doi:10.2172/1021847.
 - 13 A. Jordens, Y. P. Cheng and K. E. Waters, *Minerals Engineering*, 2013, **41**, 97 – 114.
 - 14 W. Liu, X. Wang and J. D. Miller, *Mineral Processing and Extractive Metallurgy Review*, 2019, **40**, 370–379.
 - 15 C. D. Anderson, P. R. Taylor and C. G. Anderson, *Am. J. Eng. Res.*, 2017, **6**, 155–166.
 - 16 A. G. Stack, J. E. Stubbs, S. G. Srinivasan, S. Roy, V. S. Bryantsev, P. J. Eng, R. Custelcean, A. D. Gordon and C. R. Hexel, *J. Phys. Chem. C*, 2018, **122**, 20232–20243.
 - 17 D. W. Pradip; Fuerstenau, *Miner. Metall. Process.*, 2013, **30**, 1–9.
 - 18 T.-W. Cheng, A. Partridge, T. Tran and P. Wong, *Minerals Engineering*, 1994, **7**, 1085 – 1098.
 - 19 S. G. Srinivasan, R. Shivaramaiah, P. R. C. Kent, A. G. Stack, A. Navrotsky, R. Rimani, A. Anderko and V. S. Bryantsev, *J. Phys. Chem. C*, 2016, **120**, 16767–16781.
 - 20 S. Goverapet Srinivasan, R. Shivaramaiah, P. R. C. Kent, A. G. Stack, R. Rimani, A. Anderko, A. Navrotsky and V. S. Bryantsev, *Phys. Chem. Chem. Phys.*, 2017, **19**, 7820–7832.
 - 21 B. S. Dwadasi, S. Gupta, S. Daware, S. Goverapet Srinivasan and B. Rai, *Industrial & Engineering Chemistry Research*, 2018, **57**, 17209–17217.
 - 22 S. Roy, M. D. Baer, C. J. Mundy and G. K. Schenter, *J. Chem. Phys. C*, 2016, **120**, 7597–7605.
 - 23 Y. Lee, D. Thirumalai and C. Hyeon, *J. Am. Chem. Soc.*, 2017, **139**, 12334–12337.
 - 24 S. Roy, M. Galib, G. K. Schenter and C. J. Mundy, *Chem. Phys. Lett.*, 2018, **692**, 407–415.
 - 25 S. Roy and V. S. Bryantsev, *J. Phys. Chem. B*, 2018, **122**, 12067–12076.
 - 26 S. Ramos, G. W. Neilson, A. C. Barnes and P. Buchanan, *J. Chem. Phys.*, 2005, **123**, 214501.
 - 27 S. Ansell, A. Barnes, P. Mason, G. Neilson and S. Ramos, *Biophysical Chemistry*, 2006, **124**, 171 – 179.
 - 28 P. E. Mason, S. Ansell, G. W. Neilson and S. B. Rempe, *J. Phys. Chem. B*, 2015, **119**, 2003–2009.
 - 29 E. Duboué-Dijon, P. E. Mason, H. E. Fischer and P. Jungwirth, *J. Phys. Chem. B*, 2017, **122**, 3296–3306.
 - 30 Y. Kameda, S. Maeda, Y. Amo, T. Usuki, K. Ikeda and T. Otomo, *J. Phys. Chem. B*, 2018, **122**, 1695–1701.
 - 31 V.-T. Pham and J. L. Fulton, *Journal Solution Chemistry*, 2016, **45**, 1061–1070.
 - 32 M. Galib, M. D. Baer, L. B. Skinner, C. J. Mundy, T. Huthwelker, G. K. Schenter, C. J. Benmore, N. Govind and J. L. Fulton, *J. Chem. Phys.*, 2017, **146**, 084504.
 - 33 M. Nagasaka, H. Yuzawa and N. Kosugi, *J. Phys. Chem. B*, 2017, **121**, 10957–10964.
 - 34 M. Galib, G. K. Schenter, C. J. Mundy, N. Govind and J. L. Fulton, *J. Chem. Phys.*, 2018, **149**, 124503.
 - 35 M. Benfatto, E. Pace, N. Sanna, C. Padrin and G. Chillemi, *MXAN and Molecular Dynamics: A New Way to Look to the XANES (X-ray Absorption Near Edge Structure) Energy Region*, Springer International Publishing, 2018, pp. 197–219.
 - 36 V.-T. Pham and J. L. Fulton, *Journal of Electron Spectroscopy and Related Phenomena*, 2018, **229**, 20 – 25.
 - 37 D. Zhuang, M. Riera, G. K. Schenter, J. L. Fulton and F. Paesani, *J. Phys. Chem. Lett.*, 2019, **10**, 406–412.
 - 38 R. Buchner, T. Chen and G. Hefter, *J. Phys. Chem. B*, 2004, **108**, 2365–2375.
 - 39 H. Bian, H. Chen, Q. Zhang, J. Li, X. Wen, W. Zhuang and J. Zheng, *J. Phys. Chem. B*, 2013, **117**, 7972–7984.
 - 40 K. J. Tielrooij, N. Garcia-Araez, M. Bonn and H. J. Bakker, *Science*, 2010, **328**, 1006–1009.
 - 41 D. E. Moilanen, D. Wong, D. E. Rosenfeld, E. E. Fenn and M. D. Fayer, *Proc. Natl. Acad. Sci. USA*, 2009, **106**, 375–380.
 - 42 S. Park, D. E. Moilanen and M. D. Fayer, *J. Phys. Chem. B*, 2008, **112**, 5279.
 - 43 M. D. Fayer, D. E. Moilanen, D. Wong, D. E. Rosenfeld, E. E. Fenn and S. Park, *Acc. Chem. Res.*, 2009, **42**, 1210.
 - 44 J. Lim, K. Park, H. Lee, J. Kim, K. Kwak and M. Cho, *J. Am. Chem. Soc.*, 2018, **140**, 15661–15667.
 - 45 J. A. Fournier, W. Carpenter, L. De Marco and A. Tokmakoff, *J. Am. Chem. Soc.*, 2016, **138**, 9634–9645.
 - 46 S. Roy, S. M. Gruenbaum and J. L. Skinner, *J. Chem. Phys.*, 2014, **141**, 22D505.
 - 47 S. Roy, D. Skoff, D. V. Perroni, J. Mondal, A. Yethiraj, M. K. Mahanthappa, M. T. Zanni and J. L. Skinner, *J. Am. Chem. Soc.*, 2016, **138**, 2472–2475.
 - 48 K.-i. Inoue, P. C. Singh, S. Nihonyanagi, S. Yamaguchi and T. Tahara, *J. Phys. Chem. Lett.*, 2017, **8**, 5160–5165.
 - 49 O. Kel, A. Tamimi, M. C. Thielges and M. D. Fayer, *J. Am. Chem. Soc.*, 2013, **135**, 11063.
 - 50 W. H. Casey and C. Ludwig, *Chemical Weathering Rates Of*

- Silicate Minerals*, 1995, **31**, 87–117.
- 51 J. R. Rustad, J. S. Loring and W. H. Casey, *Geochimica et Cosmochimica Acta*, 2004, **68**, 3011 – 3017.
- 52 E. Mamontov, D. J. Wesolowski, L. Vlcek, P. T. Cummings, J. Rosenqvist, W. Wang and D. R. Cole, *J. Phys. Chem. C*, 2008, **112**, 12334–12341.
- 53 A. G. Stack, J. M. Borreguero, T. R. Prisk, E. Mamontov, H.-W. Wang, L. Vlcek and D. J. Wesolowski, *Phys. Chem. Chem. Phys.*, 2016, **18**, 28819–28828.
- 54 J. Wang, J. R. Rustad and W. H. Casey, *Inorganic Chemistry*, 2007, **46**, 2962–2964.
- 55 G. Kresse and J. Hafner, *Phys. Rev. B*, 1993, **47**, 558–561.
- 56 G. Kresse and J. Hafner, *Phys. Rev. B*, 1994, **49**, 14251–14269.
- 57 G. Kresse and J. Furthmüller, *Comp. Mater. Sci.*, 1996, **6**, 15 – 50.
- 58 G. Kresse and J. Furthmüller, *Phys. Rev. B*, 1996, **54**, 11169–11186.
- 59 P. E. Blöchl, *Phys. Rev. B*, 1994, **50**, 17953–17979.
- 60 G. Kresse, *Physical Review B*, 1999, **59**, 1758–1775.
- 61 J. P. Perdew, K. Burke and M. Ernzerhof, *Phys. Rev. Lett.*, 1996, **77**, 3865–3868.
- 62 J. P. Perdew, K. Burke and M. Ernzerhof, *Phys. Rev. Lett.*, 1997, **78**, 1396–1396.
- 63 S. Grimme, J. Antony, S. Ehrlich and H. Krieg, *J. Chem. Phys.*, 2010, **132**, 154104.
- 64 A. Bankura, A. Karmakar, V. Carnevale, A. Chandra and M. L. Klein, *J. Phys. Chem. C*, 2014, **118**, 29401–29411.
- 65 C. Adamo and V. Barone, *J. Chem. Phys.*, 1999, **110**, 6158–6170.
- 66 P. Pulay, *Chem. Phys. Lett.*, 1980, **73**, 393 – 398.
- 67 Medea(R)-2.20;, *Materials Design, I.: Angel Fire, NM, USA*, 2016.
- 68 G. Wulff, *Z. Kristallogr. Mineral.*, 1901, **34**, 449–530.
- 69 L. B. Skinner, C. Huang, D. Schlesinger, L. G. M. Pettersen, A. Nilsson and C. J. Benmore, *J. Chem. Phys.*, 2013, **138**, 074506.
- 70 S. Roy, M. D. Baer, C. J. Mundy and G. K. Schenter, *J. Chem. Theory Comput.*, 2017, **13**, 3470–3477.
- 71 D. Truhlar, *Variational transition state theory and multidimensional tunneling for simple and complex reactions in the gas phase, solids, liquids, and enzymes*, in *Isotope effects in chemistry and biology*, Marcel Dekker Inc, New York, 2006, pp. 579–619.
- 72 G. K. Schenter, B. C. Garrett and D. G. Truhlar, *J. Chem. Phys. B*, 2001, **105**, 9672.
- 73 H. Kramers, *Physica*, 1940, **7**, 284–304.
- 74 R. F. Grote and J. T. Hynes, *J. Chem. Phys.*, 1980, **73**, 2715.
- 75 D. Chandler, *J. Chem. Phys.*, 1978, **68**, 2959–2970.
- 76 B. Peters, *Chem. Phys. Lett.*, 2012, **554**, 248–253.
- 77 L. D. Landau, *Physik. Z. Sowjet.*, 1932, **2**, 46.
- 78 C. Zener, *Proc. R. Soc. London*, 1932, **137**, 696–702.
- 79 M. D. Newton and N. Sutin, *Ann. Rev. Phys. Chem.*, 1984, **35**, 437–480.
- 80 S. U. M. Khan and Z. Y. Zhou, *J. Chem. Phys.*, 1990, **93**, 8808–8815.
- 81 D. Richens, *The Chemistry of Aqua Ions: Synthesis, Structure and Reactivity: A Tour Through the Periodic Table of the Elements*, Wiley, 1997.
- 82 D. Laage and J. T. Hynes, *J. Phys. Chem. B*, 2008, **112**, 7697–7701.
- 83 Y. Ni, S. M. Gruenbaum and J. L. Skinner, *Proc. Natl. Acad. Sci. USA*, 2013, **110**, 1992.